Impact of Highly Concentrated Alkaline Treatment on Mesostructured Cobalt Oxide for the Oxygen Evolution Reaction

*Eko Budiyanto, Cristina Ochoa-Hernández, and Harun Tüysüz**

Commercial alkaline water electrolysis cells typically use highly concentrate KOH as electrolyte, which strongly influences alteration of catalyst and its performance. Herein, the impact of alkaline treatment toward the structural alteration and electrochemical oxygen evolution reaction (OER) activity of well-defined ordered mesoporous Co_3O_4 is systematically studied. The overall morphology of mesostructured Co_3O_4 is relatively resilient to the exposure of highly concentrated alkaline solution up to 13 M KOH. The spectroscopic analyses, including in situ diffuse reflectance infrared spectroscopy, reveal the presence of carbonate-based species after the alkaline treatment due to impurities of the commercial KOH. The pre-treated samples exhibit a higher electrochemically active surface area, decreased charge transfer resistance, and increased current density from 103 to 155 mA cm^{-2} at 1.7 V versus RHE. The in situ electrochemical Raman spectroscopy investigation supports formation of active CoOOH phase on KOH pre-treated Co_3O_4, which might play a key role toward enhanced OER activity.

1. Introduction

The scale-up of sustainable green hydrogen production is a key point to achieve a net-zero carbon emission. The green hydrogen is industrially produced through the electrochemical water splitting process by utilizing electricity supply from the renewable energy sources; such as solar cell, wind turbines, and hydroelectric.[1] Among the electrochemical water splitting methods, the alkaline water electrolysis is the most mature technology and has been commercialized for large-scale applications. In the practical alkaline water electrolysis setup, a concentrated (7.5 M) KOH or NaOH solution is employed as the electrolyte and the cell is operated at 60–80 °C and 500 mA cm^{-2} current density with a porous diaphragm to separate the cathodic and anodic side.[2,3] Hence, the fabrication of an active and stable catalyst material is essential to fulfill the harsh operating conditions in an alkaline water electrolyzer. The utilization of highly concentrated KOH solution could alter the morphology and surface structure of the electrocatalyst even prior to the implementation of potential bias.[4] Further, the commercial reagent grade KOH pellet mostly only contains circa 85% of KOH; hence, the presence of impurities could be prominent on the electrocatalyst and the reaction when the concentrated KOH solution is used as an electrolyte.

Cobalt oxide spinel is one of the most studied electrocatalysts for oxygen evolution reaction (OER) in the recent decade owing to its tunable morphology and electronic structure.[5–15] However, the spinel phase is not the real catalyst for OER since its surface undertakes a transformation into an oxyhydroxide intermediate active state upon the anodic polarization.[9,16] This phase transformation might take place only at several or sub-nanometers regions of the catalyst surface, within the vicinity of electrode and electrolyte interfaces. Strasser et al. reported that sub-nanometer shell of the Co_3O_4 was reversibly transformed into an amorphous $CoO_x(OH)_y$ which comprises di–μ–oxo bridged $Co^{3+/4+}$ ions during the OER.[6] This surface amorphization returns to the stable crystalline phase at the resting condition. Therefore, tailoring the surface of this cobalt oxide is a sound strategy to improve its OER activity.

Following this direction, Chen and co-workers designed a Co_3O_4@CoO single crystal by reducing the surface of the Co_3O_4 with $NaBH_4$.[17] The rocksalt CoO thin surface layer acts as the active phase for OER by transforming into a CoOOH intermediate phase upon anodic polarization, while the underlying spinel phase is retained stable. Recently, Kleitz et al. reported the formation of metal hydroxylated surface upon post-treatment of various mesoporous transition metal oxides with 0.1 M $NaBH_4$.[18] The post-treated samples were proven to have metal and oxygen divacancies ($\nu_{Co} + \nu_O$) along with the formation of metal-hydroxylated surface that could enhance both OER and oxygen reduction reaction (ORR) activity. Add to this, several studies validated that the amorphous cobalt oxides have a better OER activity compared to their crystalline counterparts.[19–23]

E. Budiyanto, C. Ochoa-Hernández, H. Tüysüz
Department of Heterogeneous Catalysis
Max-Planck-Institut für Kohlenforschung
Kaiser-Wilhelm-Platz1, 45470 Mülheim an der Ruhr, Germany
E-mail: tueysuez@kofo.mpg.de

The ORCID identification number(s) for the author(s) of this article can be found under https://doi.org/10.1002/adsu.202200499.

DOI: 10.1002/adsu.202200499

Dau et al. further pointed out that the OER on amorphous and hydrated cobalt oxide does not take place exclusively at the bulk oxide/bulk electrolyte surface but throughout the hydrated oxide material.[24] The phase transformation on the surface of cobalt oxide could also be induced without the applied potential bias. Recently, Seidel and co-workers demonstrated a reversible water-induced phase change at the surface of CoO_x.[25] Near ambient pressure X-ray photoelectron spectroscopy (NAP-XPS) revealed a reversible phase change that had already taken place upon absorption of the few-monolayer thick water film whereby the nanoparticle shell was altered into octahedrally coordinated Co^{2+} and partially oxidized octahedrally coordinated Co^{3+}.

Despite the efforts, the impact of highly concentrated alkaline electrolyte solution toward the alteration of the cobalt oxide-based electrocatalyst is not systematically studied. Numerous works have reported the impact of iron impurities in ppm level toward the OER enhancement on nickel-based catalysts.[26–29] However, more tangible impurities exist in the form of carbonate (already at percent level) in the reagent grade KOH pellets that have not been explored yet.[30] The harsh conditions on the alkaline water electrolyzer could lead to a severe surface alteration on the catalyst even before the anodic polarization.

Herein, the impact of concentrated alkaline treatment (4–13 м KOH) toward the alteration of electrocatalyst structure and its OER activity is studied by using well-defined ordered mesoporous Co_3O_4 as a model system. The detailed structural analyses indicated that mesoporous framework structure is well-retained while spectroscopic analyses revealed alteration of the surface structure and presence of carbonate groups after alkaline treatment. This affected noticeably to the OER activity of the electrocatalysts. A complementary electrochemical in situ Raman spectroscopy and post-mortem study showed that the bulk material of spinel phase was preserved under OER working potential; though, changes in the surface layer might differ under the operating OER conditions.

2. Results and Discussion

The sample series of alkaline treated cobalt oxides have been prepared by immersing the as-synthesized mesoporous Co_3O_4 in 4, 8, and 13 м KOH aqueous solutions overnight (labeled as Co_3O_4-4 м, Co_3O_4-8 м, and Co_3O_4-13 м, respectively). This treatment step could also be integrated during the removal of silica hard template with an alkaline solution; hence the synthesis, as well as post-treatment, could be done in a single sequence.

High resolution transmission electron microscopy (HR-TEM) images were recorded to visualize the surface alteration of mesoporous Co_3O_4. The as-synthesized mesoporous Co_3O_4 (**Figure 1**a) shows a high crystallinity without a noticeable amorphous layer on the surface. However, the buildup of amorphous layers at sub-nanometer scale is observed on the surface of the mesoporous Co_3O_4 after highly concentrated alkaline treatment and most pronouncedly found on Co_3O_4-13 м (Figure 1b–d), denoting the alteration of the spinel surface upon immersion in the concentrated KOH solutions. Nevertheless, the low magnification TEM images reveal that the overall morphology and framework of the mesostructured Co_3O_4 are maintained and there is no visible bulk structure or aggregation due to the collapse of the mesoporous structure by alkaline treatment (Figure S1, Supporting Information).

Wide-angle XRD measurements reveal that the spinel structure is dominating the bulk structure of the material (Figure S2a, Supporting Information). The background shake-up corresponding to the amorphous species is also barely observable due to the formation of the amorphous phase only at several atomic

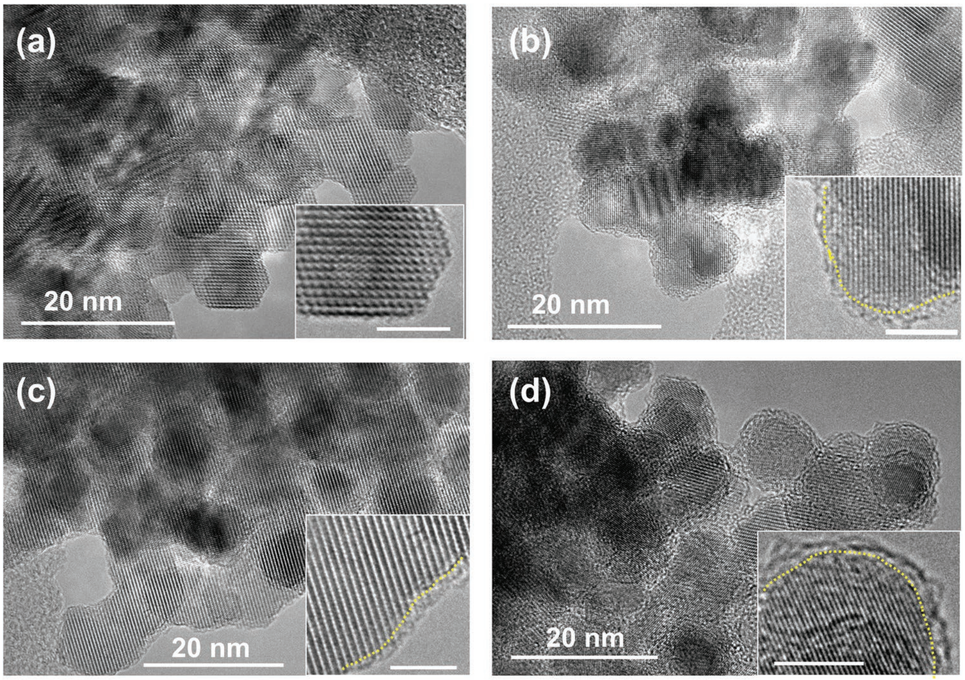

Figure 1. HR-TEM images of a) pristine Co_3O_4, b) Co_3O_4-4 м, c) Co_3O_4-8 м, and d) Co_3O_4-13 м. The scale bar in the inset is 4 nm.

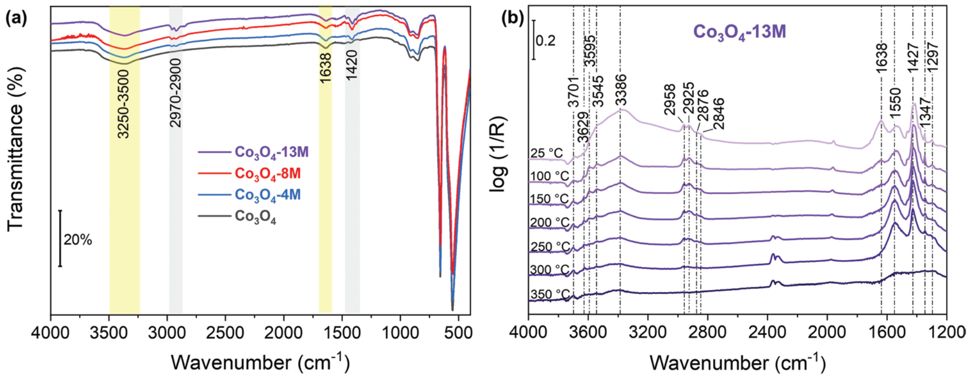

Figure 2. a) ATR-FTIR spectra of pristine Co_3O_4 and after treatment of KOH with varied concentrations. b) In situ DRIFT spectra of selected Co_3O_4-13 м at different temperatures (the values indicated in (b) correspond to the spectrum recorded at 200 °C).

layers (sub-nanometer) as shown by the HR-TEM images. Further measurements with low-angle XRD (Figure S2b, Supporting Information) show that all samples exhibit $Ia\overline{3}d$ symmetry corresponding to the perfect replication of the KIT-6 template with the characteristic (211) and (220) reflections.[31] Therefore, the KOH treatment does not noticeably influence the degree of ordering and the domain symmetry.

Next, attenuated total reflectance-Fourier transform infrared (ATR-FTIR) spectroscopy is used to investigate the vibrational groups of the materials. As seen in **Figure 2**a, all samples have two distinct peaks at 547 and 655 cm^{-1} that can be assigned to Co—O vibrations in the octahedral and tetrahedral sites of the Co_3O_4 spinel lattice, respectively.[32] The presence of water is confirmed by the characteristic bands at 3250–3500 cm^{-1} and 1638 cm^{-1}. The first one is associated with O—H stretching vibrations, being broad due to the existence of hydrogen bonds, while the latter is attributed to the bending of water molecules.[33,34] Moreover, when the concentration of KOH increases, new bands around 2700–2900 cm^{-1} and 1420 cm^{-1} appear. The first region is ascribed to C—H stretching vibrations that hint the existence of some organic species, while the second band is associated with carbonates. Both are related to impurities in the reagent grade commercial KOH pellets.[30]

Temperature-dependent in situ diffuse reflectance infrared Fourier transform (DRIFT) spectroscopy is used to get further insights into the hydroxyl groups and the stability of the carbonate species on the selected pristine Co_3O_4 and Co_3O_4-13 м samples. As seen in Figure 2b, after removing most of the physisorbed water (1638 cm^{-1}) at 200 °C, the stretching vibrations of OH bond become more visible (3750–3500 cm^{-1}) on the surface of Co_3O_4-13 м. The bands at 3701 and 3629 cm^{-1} can be attributed to surface OH groups bonded to one or two cobalt atoms, respectively.[35] While highly perturbated OH groups could be the reason of the broad band at 3386 cm^{-1}, no accurate assignments can be done for the bands at 3595 and 3545 cm^{-1}. Considering the surface analysis of other oxides, these bands could be related to triply-bridging OH groups or H-bond species.[36,37] A similar profile of OH groups is observed for the pristine Co_3O_4 sample (Figure S3, Supporting Information). However, some distinct differences are visible in the range of 1600–1200 cm^{-1}. A portion of carbonate species could also be detected within this sample, most probably due to the presence of carbonate impurities in the commercial reagent grade NaOH that was used for silica leaching during the nanocasting process. Nevertheless, the intensity of these bands is much stronger in the case of Co_3O_4-13 м. As shown by Figure 2b, the absorption bands at 1427 and 1347 cm^{-1} reveal the presence of polydentate carbonates ($\Delta\nu_3<250$), which exhibit high thermal stability.[38–40] In addition, two more bands are observed at 1550 and 1297 cm^{-1} that could be attributed to bidentate carbonates ($\Delta\nu_3>250$).[39,40] However, the band in the region of 1590–1530 cm^{-1} could be also related to the ν_{as}(COO) vibration mode of formate and acetate species.[35,38] The presence of these organic impurities was also confirmed by the high-performance liquid chromatography (HPLC) analysis on 13 м KOH solution. This goes also in line with the presence of C—H stretching vibrations in the range of 3000–2800 cm^{-1}. Therefore, the coexistence of different species could not be ruled out since the C—H bands disappear at lower temperature than the band at 1550 cm^{-1}. Carbonate decomposition takes place between 250 and 350 °C. When these bands start to fade away, simultaneously two new bands arise at 2363 and 2330 cm^{-1} corresponding to released CO_2. However, the exact amount of carbonates could not be assessed by the thermogravimetric mass spectra (TG-MS) due to the overlapping with the release of hydroxyl groups at similar temperature range. Nevertheless, the total content of carbonate and hydroxyl groups on the surface released at this temperature range is about 2.9 wt% (Figure S4, Supporting Information). Overall, IR spectroscopy analysis clearly indicates surface alteration through adsorption of carbonate and some organic species associated with the impurity of commercial KOH.

The nitrogen physisorption analysis was further performed to investigate the specific surface area, pore volume, and the pore size distribution of the samples (Figure S5 and Table S1, Supporting Information). The typical type IV isotherm, which is characteristic of mesoporous materials, and pore size distribution of the materials are retained after the KOH treatments. In addition, there is no significant change in the determined BET surface area and pore volume. All in all, the TEM analysis and textural characterization support that the mesoporous framework is robust to the harsh alkaline treatment.

A surface-sensitive XPS study was then carried out to analyze the oxidation state and composition of the as-generated amorphous layer. The overlay of high resolution Co 2p scan and the evaluation from satellite peaks (Figure S6a–e, Supporting Information) resemble the characteristic profile of Co_3O_4, which contains Co^{2+} and Co^{3+} oxidation states.[41,42] Hence, alkaline treatment did not significantly change the oxidation state of cobalt. Nonetheless, the peak corresponding to hydroxide could be found from the O 1s peak deconvolution (labeled as II in Figure S7a–d, Supporting Information).[42] The existence of the hydroxide on the surface originated from the harsh alkaline treatment, either during the treatment with higher KOH concentration or during the silica template removal step with 2 M NaOH at 70 °C. The surface hydroxyl groups appear at 531.7–532.0 eV (labeled as III).[42,43] The discrepancy of O 1s deconvoluted peak at 532.5–533.0 eV (labeled as IV) is only observed on the samples after KOH treatment (Figure S7a–d, Supporting Information), which originated from surface contamination by carbonate and other organic species impurities in the commercial reagent grade KOH pellets as also supported by IR spectroscopy analysis.[44]

Following the structural characterization, the catalytic activity of the materials is screened in the electrochemical OER in a 1 M KOH electrolyte. The stabilized linear sweep voltammetry (LSV) curves by 50 cycles of cyclic voltammetry (CV) scan show a clear trend of increasing activity with the increasing of KOH concentration during the treatment (**Figure** 3a,b). An enhancement of current density at 1.7 V versus RHE from 103 to 155 mA cm^{-2} as well as a decrease of overpotential at 10 mA cm^{-2} from 401 to 394 mV is obtained for Co_3O_4-13 M compared to the pristine Co_3O_4.

However, a volcano plot correlation could not be derived due to the limitation on the concentration of KOH solution, which, is already close to its saturation point. To validate the reproducibility of the OER activity, a second batch of Co_3O_4 sample was prepared by treating with 13 M KOH and tested with three different working electrodes (WEs). As shown in Figure S8, Supporting Information, sample from both batches show an identical activity, denoting the reproducible impact of this alkaline treatment to its OER activity. Both pristine Co_3O_4 and the most active sample (Co_3O_4-13 M) are slightly deactivated after stabilization by 50 CV scans (Figure S9, Supporting Information). This hints that the iron impurities in commercial 1 M KOH solution do not have activation effect on this catalyst system, as also observed in our previous studies on mesostructured Co_3O_4.[26,45]

A control experiment has been conducted by re-calcining the Co_3O_4-13 M at 400 °C in air to remove surface carbonate and organic species as investigated by the aforementioned temperature-dependent in situ DRIFTS analysis. As seen in ATR-FTIR spectra in Figure S10a, Supporting Information, carbonates, and organic species could be mainly removed by re-calcination at 400 °C. The sample after re-calcination at 400 °C exhibits an identical OER activity to the as-prepared Co_3O_4-13 M (Figure S10b, Supporting Information). This hints that the adsorbed carbonates and C—H species could be totally oxidized under applied potential bias or these species could be removed from the surface of the Co_3O_4 when it was immersed into electrolyte and have minimum impact to OER activity.[46]

A kinetic analysis was further conducted by calculating Tafel slope, as shown in Figure 3c. The calculated Tafel slopes for all samples are within the range of 48–50 mV dec^{-1}, which are the typical values for cobalt oxide materials following a single site reaction mechanism with Co^{3+} to Co^{4+} oxidation at Co—Co di–μ–oxo bridge as the rate-determining step.[47–49] To shed light

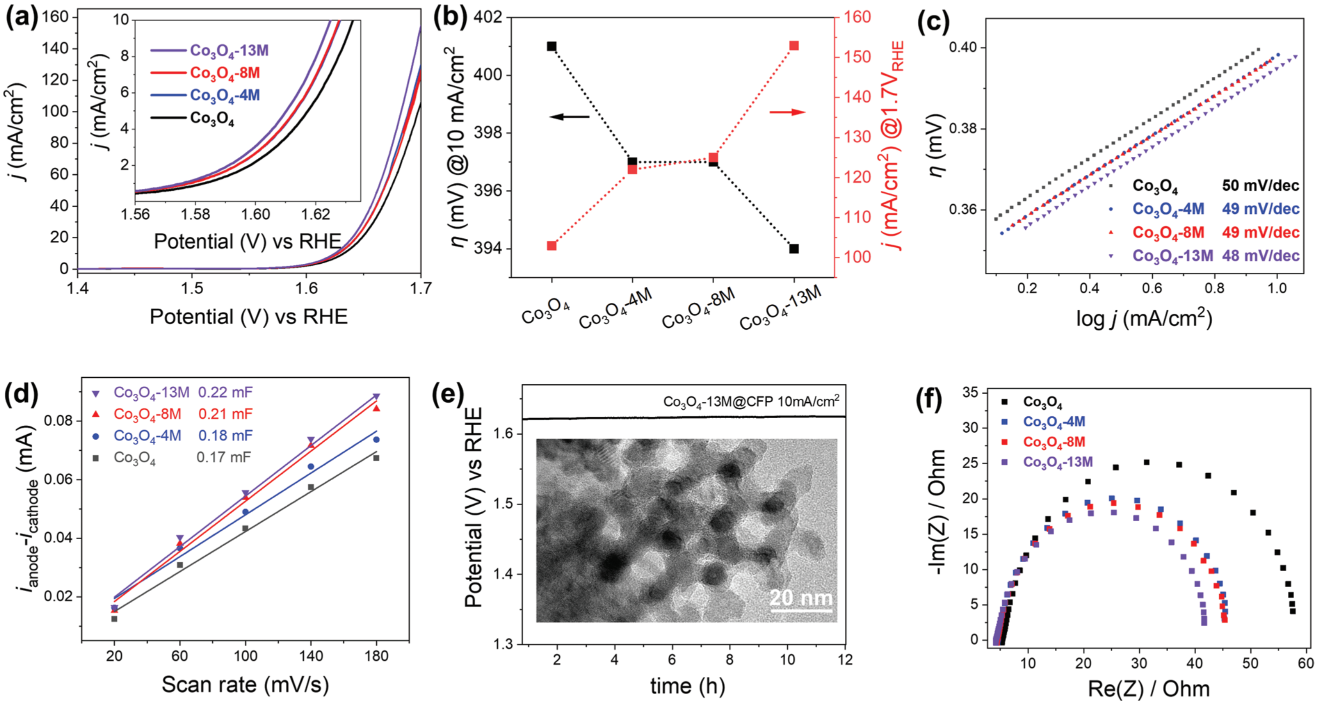

Figure 3. OER performances of Co_3O_4 and KOH treated sample series: a) LSV curves on OER in 1 M KOH solution with the inset of the enlarged region of overpotential at 10 mA cm^{-2}, b) summary of current density at 1.7 V versus RHE and overpotential at 10 mA cm^{-2}, c) kinetic measurement by Tafel slope, d) plots of anodic and cathodic current difference recorded at 1.05 V versus RHE at varying scan rates, e) chronopotentiometry (CP) at 10 mA cm^{-2} over 12 h with the corresponding TEM micrograph of the catalyst scratched from working electrode, and f) Nyquist plots.

into the origin of the catalytic enhancement by the KOH treatment, the electrochemical surface area (ECSA) was calculated based on the electrical double-layer capacitance (EDLC) at the non-Faradaic region.[50] As seen in Figure 3d and the summary of OER measurements in Table S2, Supporting Information, the ECSA is enhanced from 4.25 cm^2 to 5.5 cm^2 by the KOH treatment. The ECSA normalized current density showed a comparable intrinsic activity on all samples, denoting the similarity of the intermediate active species (Figure S11, Supporting Information). It goes in line with the similar value of the aforementioned Tafel slopes that could be translated into an uniform rate-determining step for all samples. Hence, the activity enhancement after alkaline treatment could be rather related to the higher surface area of active sites under applied potential bias. This indicates the essential role of KOH treatment to alter the surface structure of the Co_3O_4 that might affect the formation of surface intermediate active sites under operating OER condition, which will be further discussed below in the in situ electrochemical Raman spectroscopy section.

The chronopotentiometry (CP) test at 10 mA cm^{-2} was further carried out to investigate the stability of the catalyst upon a prolonged potential bias. As seen in Figure 3e, the most active catalyst (Co_3O_4-13 м) does not show a tangible deactivation and has a good stability up to 12 h. The catalyst also presents a good morphological stability and indication of surface reconstruction after applied potential bias as shown by the HR-TEM image (Figure S12a, Supporting Information). The absence of observable change in the Raman spectra prior to and after the reaction (Figure S12b, Supporting Information) denotes the bulk catalyst is robust to the reaction condition.

The charge transfer capability of the electrocatalyst was further evaluated by measuring the electrochemical impedance spectroscopy (EIS) as shown in Figure 3f. The as-measured Nyquist plots were then fitted to the Randles model (R_Ω) $(Rct \cdot Qdl)$ as shown in Figure S13a, Supporting Information. The EIS fitting result (Figure S13b–e and Table S2, Supporting Information) shows a decreasing trend of charge transfer resistance after the KOH treatment. The value is decreased from 53.4 Ω for pristine Co_3O_4 to 38.0 Ω for Co_3O_4-13 м. This could be correlated to the enhanced electron transfer on the electrical double layer on KOH treated samples. As a result, not only the charge transfer resistance could be decreased, but it also contributes to the increase of ECSA value.

To evaluate the efficiency of oxygen production and charge utilization, the Faradaic efficiency (FE) measurements were conducted following the rotating-ring disc electrode (RRDE) method proposed by Jaramillo.[50] As shown in Figure S14, Supporting Information, a slight deviation from 100% utilization is observed on all samples that could be related to the side reaction of carbon oxidation from the Nafion binder or other organic species on the surface.[46] Nevertheless, a higher FE could be observed in the KOH treated samples. This could be ascribed to the more efficient charge utilization due to the surface alteration by highly concentrated alkaline treatment. Note that under OER working potential, the surface of the spinel phase needs to be transformed into an (oxy)hydroxide phase, hence it consumes an extra charge for this transformation.[9,47] The surface alteration due to the pre-treatment with KOH is apparently able to speed up the formation of intermediate active state, therefore it is translated into a higher charge utilization for oxygen production.

To monitor a possible alteration of Co_3O_4 upon applied potential bias, in situ electrochemical Raman spectroscopy study is conducted by using a home-made flow cell (Figure S15, Supporting Information), and depositing Co_3O_4-13 м on roughened Au substrate as the WE. For this experiment, 0.1 м KOH aqueous solution was used as electrolyte to avoid quick bubbles formation during the measurement and ensure the spectra with good signal-to-noise ratio.[47,51] The CV scan conducted with the blank Au shows that the substrate has a negligible OER activity compared to the sample (Figure S16, Supporting Information). The Raman spectra of the Co_3O_4-13 м sample show five well-resolved Raman bands that are typical for spinel phase (**Figure 4**a).[52,53] The first F_{2g} band at around 200 cm^{-1} was not shown due to the overlapping with diffuse scattering of the electrolyte solution at low wavenumbers.[54]

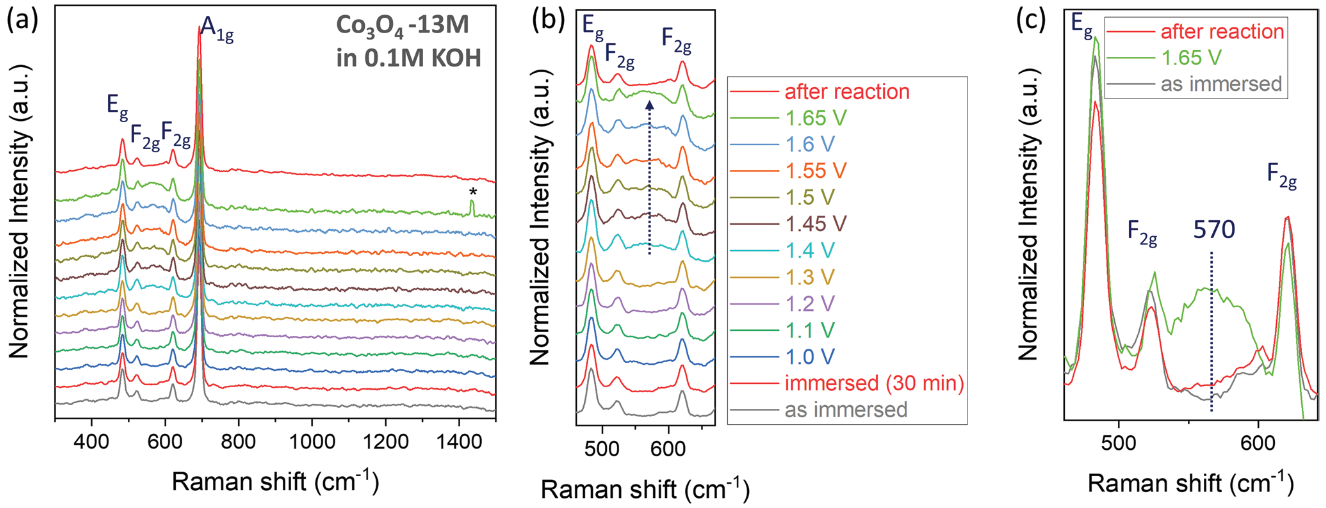

Figure 4. a) In situ Raman spectra of the Co_3O_4-13 м sample measured in a 0.1 м KOH electrolyte within 0.05 or 0.1 V potential step. b) Magnification of the band corresponding to hydroxylated species. c) Comparison of spectra before reaction, under OER, and after reaction within the interested region. The asterisk in (a) indicates the peak from cosmic ray.

As next, a gradual increase of potential was then applied in chronoamperometry (CA) mode and the in situ Raman spectra were collected. As seen in Figure 4a, well-resolved Raman bands belonging to the Co_3O_4 spinel phase were retained during the electrochemical measurements.[52] This shows that the underlying spinel phase could offer a highly stable scaffold to the hydroxylated amorphous phase thereon. The evolution of oxyhydroxide phase that appears as a hump centered at 570 cm^{-1} from 1.45 V versus RHE (Figure 4b, see also the reference spectra of CoOOH in Figure S17, Supporting Information) is observed during the in situ measurement.[16,41,55,56] To distinguish this peak from the Au–O stretching vibration of Au oxide,[16] the blank measurement was then conducted with roughened Au as the WE.

As shown in Figure S18a, Supporting Information, the broad shake-up peak at around 500 cm^{-1} was observed on Au under potential bias. However, a clear peak shape and intensity difference could be observed at around 570 cm^{-1} when the spectra of blank Au and Co_3O_4-13 м at 1.65 V_{RHE} are directly confronted (Figure S18b, Supporting Information). Hence, this peak could be assigned to the as-formed CoOOH species. Taking into account the thick deposition of sample powder on the Au substrate, hence the spectral contribution of the underlying Au might be minimized, and the measured spectra resemble the cobalt oxide surface.[55] The recorded spectra have a similarity to the Raman spectra of pure Co surface reported by Bell et al.[16]

Add to that, the peak centered at 570 cm^{-1} evolved earlier on Co_3O_4-13 м (Figure 4b) and is more pronounced compared to pristine Co_3O_4 (Figure S19a–c, Supporting Information), denoting the surface alteration after highly concentrated alkaline solution treatment might enhance the formation of oxyhydroxide intermediate and decrease the visible onset potential, as-observed in LSV curve (Figure 3a).[57] The evolution of the peak corresponding to CoOOH from 1.45 V versus RHE is in agreement with the observed anodic peak from CV scan (Figure S16, Supporting Information). This also fits with the stability of CoOOH phase in water environment at 25 °C and pH 13 as proposed by the Pourbaix diagram.[58] This generated CoOOH phase is the intermediate active phase for OER as the peak at 570 cm^{-1} disappeared once the potential bias was terminated (Figure 4c).[6] The shift and broadening on the A_{1g} band at 690 cm^{-1} that could hint at the oxidation of cobalt species into Co^{4+} on the surface of the electrocatalyst, as proposed by Jin et al.,[56] could not be observed by us. This is due to the large domain size and thick deposition of powder sample on the substrate that might decrease the surface sensitivity of SERS experiment and contribution of resilient Co_3O_4 underneath.[55]

3. Conclusion

The impact of highly concentrated alkaline treatment has been studied by treating the ordered mesoporous Co_3O_4 with the variation of KOH concentration. After the KOH treatment, the systematic structural analyses through HR-TEM, XRD, physisorption, XPS, and ATR-FTIR studies reveal the preservation of the crystalline and mesoporous framework structures. The presence of carbonate, as well as organic species due to the impurities from the commercial reagent grade KOH pellets, were also verified. The detailed OER study discloses the inherent activity increase with the concentration of KOH solution during the treatment of the catalyst materials. In situ electrochemical Raman spectroscopy study supported the early formation of the active CoOOH phase on Co_3O_4-13 м compared to Co_3O_4, which might play a key role toward enhanced OER activity. This study provides an insight into the importance of reassessing the surface alteration of the catalysts prior to reaction under harsh conditions that are analogous to the industrial alkaline water electrolysis.

4. Experimental Section

Synthesis of KIT-6 Silica Template: KIT-6 silica template was prepared following the published protocol.[59] Briefly, 13.5 g of P123 (M: 5800, Sigma Aldrich) was dissolved in 487.5 g of deionized water in 1 L polypropylene bottle until homogeneous solution was obtained. Then, 26.1 g of concentrated HCl (37%, J. T. Baker) was added into the solution and stirred vigorously. The mixture was then stirred continuously at 35 °C, and in the meantime, 13.5 mL of 1-butanol was added. After 1 h of stirring, 29 g of tetraethyl orthosilicate (TEOS, 98% reagent grade, Sigma Aldrich), used as the silica source, was added into the reactor and the mixture was stirred continuously at 35 °C for 24 h. The mixture was then subjected to hydrothermal treatment at 100 °C for 24 h. The as-obtained white precipitate was filtered and washed repeatedly with ethanol and distilled water. The final product was then calcined at the final temperature of 550 °C for 6 h to remove the surfactant.

Synthesis and Post-Treatment of Mesoporous Co_3O_4: Mesoporous Co_3O_4 was synthesized via the hard-templating method by using the as-prepared KIT-6 silica as templating material. In brief, cobalt precursor ($Co(NO_3)_2{\cdot}6H_2O$, ACS reagent grade 99.5% purity, Sigma Aldrich) was dissolved in ethanol and impregnated into the pore confinement of KIT-6 silica via a two-step wet-impregnation method. The composite was stirred at room temperature for 2 h and let dry overnight on a broad petri dish at 40 °C. The as-obtained composite was then crushed and calcined at 200 °C for 4 h (heating rate 2 °C min^{-1}). After the second impregnation step, the composite was calcined at 500 °C for 6 h with an intermediate dwelling at 250 °C for 4 h (heating rate 2 °C min^{-1}). The KIT-6 silica template was then subjected to a repeated etching with 2 м NaOH at 70 °C. Then, the sample was washed with distilled water until neutral pH was reached.

For the highly concentrated KOH treatment, the as-prepared mesoporous Co_3O_4 was then immersed in KOH solution (concentration: 4, 8, and 13 м) overnight. The precipitate was then separated from the KOH solution by rounds of centrifugation at 9000 rpm and washing with distilled water until neutral pH was reached. The final product was then dried at 90 °C overnight and finely ground. The obtained samples were then labeled as Co_3O_4-4 м, Co_3O_4-8 м, and Co_3O_4-13 м.

Material Characterization: Powder XRD reflection data were measured with a STOE theta/theta diffractometer in Bragg-Brentano geometry equipped with Cu $K\alpha_{1/2}$ X-ray source with 0.03° 2 theta acquisition step at room temperature. Phase identification of the experimental XRD pattern was referred to the PDF-2 ICCD database.[60] Nitrogen physisorption measurements were performed with 3Flex Micromeritics setup at 77 K. The sample was degassed at 150 °C for 10 h prior to the physisorption measurement. Brunauer–Emmett–Teller (BET) surface area was calculated within the 0.06 to 0.3 relative pressure range ($p/p°$). Pore size distribution was calculated with Barrett, Joyner, and Halenda's (BJH) method.

ATR-FTIR spectra were measured with a Perkin-Elmer Spectrum Two spectrometer with 16 scans spectra acquisition. Temperature dependence of the surface groups was evaluated by DRIFT spectroscopy. A Harrick Praying Mantis accessory equipped with a high temperature reaction chamber with KBr windows was placed in a Nicolet Magna-IR 560 spectrometer. Before every experiment, the sample was flushed with an inert gas (10 mL min^{-1}) at room temperature for 60 min to remove the moisture. Subsequently, the system was heated up to 350 °C with 5 °C min^{-1} ramp. Spectra were collected at different temperatures, recording 100 scans per spectrum and 4 cm^{-1} resolution with an MCT (Mercury-Cadmium-Telluride) detector. XPS data were measured with a SPECS spectrometer with a hemispherical analyzer (PHOIBOS 150). The monochromatized Al Kα (E = 1486.7 eV) at 200 W/15 kV was used as X-ray source. The narrow scans were measured with 20 eV pass energy. The lens mode was set to the medium area, and the analysis chamber was 5×10^{-10} mbar. The binding energy was corrected using the C 1s peak for adventitious carbon at 284.5 eV.

TG-MS data were collected in a Netzsch STA 449 F3 Jupiter TG instrument coupled with a Netzsch QMS 403 D Aeolos mass spectrometer. Around 10 mg of powder sample was heated from 40–500 °C at a ramping rate of 5 °C min^{-1} under Ar gas flow (40 mL min^{-1} flow rate with 20 mL min^{-1} protective flow). Analog scan mode was used to record mass spectra.

TEM micrographs were taken with a Hitachi HF-2000 instrument equipped with cold field emission gun operated at 200 kV acceleration voltage. For TEM measurements, powder samples were dry-casted onto Cu lacey carbon grid (Plano GmbH).

Electrochemical Characterization: Electrochemical OER was examined with VSP-300 potentiostat (BioLogic) in a Teflon container electrochemical cell with a three-electrode configuration using 1 м KOH as electrolyte. The cell was connected to the rotating disc electrode (RDE) setup (model: BluRev RDE, BioLogic). The Pt wire and hydrogen reference electrode (RE) (Hydroflex, Gaskatel) were employed as the counter electrode (CE) and RE, respectively. The WE was fabricated by drop-casting ink solution onto a 0.196 cm^2 glassy carbon RDE. The loading of catalyst was calculated as 0.13 mg cm^{-2}. Prior to the catalyst deposition, the glassy carbon RDE was polished with a micropolish alumina suspension (1 µm and 50 nm particle size, Buehler). Catalyst ink was prepared by ultrasonicating 4.8 mg of catalyst powder, 50 µL Nafion-117 (Sigma Aldrich), 0.75 mL of ultrapure water, and 0.25 mL isopropanol. The electrolyte solution was degassed with Ar flow.

The catalyst was then tested in the LSV in the potential range between 0.70 and 1.70 V versus RHE with scan rate of 10 mV s^{-1}. CV scan was performed at the scan rate of 50 mV s^{-1} from 0.7 to 1.6 V versus RHE. EIS was recorded at 1.6 V versus RHE within the 100 kHz and 100 mHz frequency range. Experimental Nyquist plot was then fitted to the equivalent circuit model using Z-Fit feature in EC-Lab software. EDLC or Cdl was measured by performing CV in the non-Faradaic region at varied scan rates (20 to 180 mV s^{-1}). ECSA was calculated by dividing the Cdl value with specific capacitance of electrolyte solution (0.04 mF cm^{-2}).[50] The stability test was conducted with controlled current (chronopotentiometry) at a 10 mA cm^{-2} current density. The Ohmic drop was compensated at 85%.

FE was measured with RRDE method.[50] The catalyst ink was deposited on the RRDE tip (model: PineResearch E7R9, glassy carbon disc diameter 5.61 mm, Pt ring, calibrated collection efficiency of 37.6%) to fabricate the WE. The electrolyte was degassed with Ar flow for 30 min before the measurement and then the ring background current was measured. The 0.4 V versus RHE bias was applied on the ring and the RRDE was rotated at 1600 rpm during the measurement. The FE was calculated at 1 mA cm^{-2} disc current with the following formula:

$$FE = \left(2 \cdot I_{\text{ring}}\right) / \left(I_{\text{disc}} \cdot N\right) \tag{1}$$

I_{ring} is the measured ring current, I_{disc} is constant disk current, and N is the calibrated collection efficiency for the RRDE.

In Situ Raman Spectroscopy: In situ Raman spectroscopy measurement was conducted in a homemade electrochemical flow cell with three-electrode system (Pt wire as CE, hydrogen RE, and sample deposited on the roughened Au substrate as WE). The Au foil was electrochemically roughened by adapting the previously reported protocol.[16] The sample ink was drop-casted into the roughened Au substrate and dried under Ar flow. Ar degassed 0.1 м KOH electrolyte was used as the electrolyte solution. Two consecutive scans, 12 s exposure time were used to collect the in situ spectra. Ocean Optics QE Pro-Raman spectrometer using an excitation wavelength of 785 nm and PTFE-protected Raman probe (InPhotonics) were used to record the spectra, coupled with Potentiostat (WaveNow, PINE Research Instrumentation) to control the current-potential response. The spectra were recorded during chronoamperometry measurement at given potential step and presented without the baseline subtraction nor cosmic ray removal.

Supporting Information

Supporting Information is available from the Wiley Online Library or from the author.

Acknowledgements

This research was financially supported by the Deutsche Forschungsgemeinschaft (DFG, German Research Foundation) Projektnummer 388390466-TRR247(sub-projectC1) within the Collaborative Research Centre/Transregio247 "Heterogeneous Oxidation Catalysis in the Liquid Phase," the Carbon2Chem project funded by the Bundesministerium für Bildung und Forschung (BMBF) of the German government, and by the Max Planck Society. The authors thank H. Hinrichs for the HPLC measurements and T. Beyazay for the discussion. Dr. C. Weidenthaler and S. Leiting are acknowledged for XPS measurements and data evaluation. Fine mechanics department led by W. Kersten is acknowledged for fabricating the in situ electrochemical Raman cell.

Open access funding enabled and organized by Projekt DEAL.

Conflict of Interest

The authors declare no conflict of interest.

Data Availability Statement

The data that support the findings of this study are available from the corresponding author upon reasonable request.

Keywords

cobalt oxide, in situ Raman, KOH treatment, mesoporous structures, oxygen evolution reaction

Received: November 30, 2022
Revised: January 12, 2023

[1] P. De Luna, C. Hahn, D. Higgins, S. A. Jaffer, T. F. Jaramillo, E. H. Sargent, *Science* **2019**, *364*, eaav3506.
[2] W. Ju, M. V. F. Heinz, L. Pusterla, M. Hofer, B. Fumey, R. Castiglioni, M. Pagani, C. Battaglia, U. F. Vogt, *ACS Sustainable Chem. Eng.* **2018**, *6*, 4829.
[3] M. Schalenbach, G. Tjarks, M. Carmo, W. Lueke, M. Mueller, D. Stolten, *J. Electrochem. Soc.* **2016**, *163*, F3197.
[4] C. Andronescu, S. Seisel, P. Wilde, S. Barwe, J. Masa, Y.-T. Chen, E. Ventosa, W. Schuhmann, *Chem. - Eur. J.* **2018**, *24*, 13773.
[5] A. Bergmann, T. E. Jones, E. M. Moreno, D. Teschner, P. Chernev, M. Gliech, T. Reier, H. Dau, P. Strasser, *Nat. Catal.* **2018**, *1*, 711.

[6] A. Bergmann, E. Martinez-Moreno, D. Teschner, P. Chernev, M. Gliech, J. F. de Araújo, T. Reier, H. Dau, P. Strasser, *Nat. Commun.* **2015**, *6*, 8625.
[7] H. Tüysüz, Y. J. Hwang, S. B. Khan, A. M. Asiri, P. Yang, *Nano Res.* **2013**, *6*, 47.
[8] M. Yu, E. Budiyanto, H. Tüysüz, *Angew. Chem., Int. Ed.* **2022**, *11*, e202103824.
[9] H.-Y. Wang, S.-F. Hung, Y.-Y. Hsu, L. Zhang, J. Miao, T.-S. Chan, Q. Xiong, B. Liu, *J. Phys. Chem. Lett.* **2016**, *7*, 4847.
[10] Y. Xu, F. Zhang, T. Sheng, T. Ye, D. Yi, Y. Yang, S. Liu, X. Wang, J. Yao, *J. Mater. Chem. A* **2019**, *7*, 23191.
[11] M. Yu, C. K. Chan, H. Tüysüz, *ChemSusChem* **2018**, *11*, 605.
[12] S. Lin, M. A. Habib, R. Mandavkar, R. Kulkarni, S. Burse, Y.-U. Chung, C. Liu, Z. Wang, S. Lin, J.-H. Jeong, J. Lee, *Adv. Sustainable Syst.* **2022**, *6*, 2200213.
[13] S. P. Selvam, S. Cho, *Adv. Sustainable Syst.* **2022**, *6*, 2200038.
[14] P. Wang, L. Zhang, Z. Wang, D. Bu, K. Zhan, Y. Yan, J. Yang, B. Zhao, *J. Colloid Interface Sci.* **2021**, *597*, 361.
[15] T. Tran-Phu, R. Daiyan, J. Leverett, Z. Fusco, A. Tadich, I. Di Bernardo, A. Kiy, T. N. Truong, Q. Zhang, H. Chen, P. Kluth, R. Amal, A. Tricoli, *Chem. Eng. J.* **2022**, *429*, 132180.
[16] B. S. Yeo, A. T. Bell, *J. Am. Chem. Soc.* **2011**, *133*, 5587.
[17] C.-W. Tung, Y.-Y. Hsu, Y.-P. Shen, Y. Zheng, T.-S. Chan, H.-S. Sheu, Y.-C. Cheng, H. M. Chen, *Nat. Commun.* **2015**, *6*, 8106.
[18] W. Deeloed, T. Priamushko, J. Čížek, S. Suramitr, F. Kleitz, *ACS Appl. Mater. Interfaces* **2022**, *14*, 23307.
[19] G.-h. Moon, M. Yu, C. K. Chan, H. Tüysüz, *Angew. Chem., Int. Ed.* **2019**, *58*, 3491.
[20] Y. Q. Gao, H. B. Li, G. W. Yang, *J. Appl. Phys.* **2016**, *119*, 034902.
[21] C. Pasquini, L. D'Amario, I. Zaharieva, H. Dau, *J. Chem. Phys.* **2020**, *152*, 194202.
[22] L. Gong, X. Y. E. Chng, Y. Du, S. Xi, B. S. Yeo, *ACS Catal.* **2018**, *8*, 807.
[23] A. Indra, P. W. Menezes, N. R. Sahraie, A. Bergmann, C. Das, M. Tallarida, D. Schmeißer, P. Strasser, M. Driess, *J. Am. Chem. Soc.* **2014**, *136*, 17530.
[24] K. Klingan, F. Ringleb, I. Zaharieva, J. Heidkamp, P. Chernev, D. Gonzalez-Flores, M. Risch, A. Fischer, H. Dau, *ChemSusChem* **2014**, *7*, 1301.
[25] D. Hein, G. Wartner, A. Bergmann, M. Bernal, B. R. Cuenya, R. Seidel, *ACS Nano* **2020**, *14*, 15450.
[26] X. Deng, S. Öztürk, C. Weidenthaler, H. Tüysüz, *ACS Appl. Mater. Interfaces* **2017**, *9*, 21225.
[27] L. Trotochaud, S. L. Young, J. K. Ranney, S. W. Boettcher, *J. Am. Chem. Soc.* **2014**, *136*, 6744.
[28] M. S. Burke, M. G. Kast, L. Trotochaud, A. M. Smith, S. W. Boettcher, *J. Am. Chem. Soc.* **2015**, *137*, 3638.
[29] S. Lee, L. Bai, X. Hu, *Angew. Chem., Int. Ed.* **2020**, *59*, 8072.
[30] P. Sipos, P. M. May, G. T. Hefter, *Analyst* **2000**, *125*, 955.
[31] X. Deng, W. N. Schmidt, H. Tüysüz, *Chem. Mater.* **2014**, *26*, 6127.
[32] A. N. Naveen, S. Selladurai, *Electrochim. Acta* **2014**, *125*, 404.
[33] B. L. Mojet, S. D. Ebbesen, L. Lefferts, *Chem. Soc. Rev.* **2010**, *39*, 4643.
[34] N. Shi, W. Cheng, H. Zhou, T. Fan, M. Niederberger, *Chem. Commun.* **2015**, *51*, 1338.
[35] K. Chen, W. Li, Z. Zhou, Q. Huang, Y. Liu, Q. Duan, *Catal. Sci. Technol.* **2020**, *10*, 2573.
[36] G. Busca, *Catal. Today* **2014**, *226*, 2.
[37] G. Busca, V. Lorenzelli, G. Ramis, R. J. Willey, *Langmuir* **1993**, *9*, 1492.
[38] A. Efremova, T. Rajkumar, Á. Szamosvölgyi, A. Sápi, K. Baán, I. Szenti, J. Gómez-Pérez, G. Varga, J. Kiss, G. Halasi, Á. Kukovecz, Z. Kónya, *J. Phys. Chem. C* **2021**, *125*, 7130.
[39] J. C. Lavalley, *Catal. Today* **1996**, *27*, 377.
[40] C. Binet, M. Daturi, J.-C. Lavalley, *Catal. Today* **1999**, *50*, 207.
[41] J. Yang, H. Liu, W. N. Martens, R. L. Frost, *J. Phys. Chem. C* **2010**, *114*, 111.
[42] M. C. Biesinger, L. W. M. Lau, A. R. Gerson, R. S. C. Smart, *Appl. Surf. Sci.* **2010**, *257*, 887.
[43] H. Idriss, *Surf. Sci.* **2021**, *712*, 121894.
[44] J. Stoch, J. Gablankowska-Kukucz, *Surf. Interface Anal.* **1991**, *17*, 165.
[45] M. Yu, G.-h. Moon, R. G. Castillo, S. DeBeer, C. Weidenthaler, H. Tüysüz, *Angew. Chem., Int. Ed.* **2020**, *59*, 16544.
[46] S. Möller, S. Barwe, J. Masa, D. Wintrich, S. Seisel, H. Baltruschat, W. Schuhmann, *Angew. Chem., Int. Ed.* **2020**, *59*, 1585.
[47] A. Moysiadou, S. Lee, C.-S. Hsu, H. M. Chen, X. Hu, *J. Am. Chem. Soc.* **2020**, *142*, 11901.
[48] R. D. L. Smith, C. Pasquini, S. Loos, P. Chernev, K. Klingan, P. Kubella, M. R. Mohammadi, D. Gonzalez-Flores, H. Dau, *Nat. Commun.* **2017**, *8*, 2022.
[49] J. B. Gerken, J. G. McAlpin, J. Y. C. Chen, M. L. Rigsby, W. H. Casey, R. D. Britt, S. S. Stahl, *J. Am. Chem. Soc.* **2011**, *133*, 14431.
[50] C. C. L. McCrory, S. Jung, J. C. Peters, T. F. Jaramillo, *J. Am. Chem. Soc.* **2013**, *135*, 16977.
[51] L. Bai, S. Lee, X. Hu, *Angew. Chem., Int. Ed.* **2021**, *60*, 3095.
[52] V. G. Hadjiev, M. N. Iliev, I. V. Vergilov, *J. Phys. C: Solid State Phys.* **1988**, *21*, L199.
[53] Y.-C. Liu, J. A. Koza, J. A. Switzer, *Electrochim. Acta* **2014**, *140*, 359.
[54] K. Hedenstedt, J. Bäckström, E. Ahlberg, *J. Electrochem. Soc.* **2017**, *164*, H621.
[55] Z. Chen, L. Cai, X. Yang, C. Kronawitter, L. Guo, S. Shen, B. E. Koel, *ACS Catal.* **2018**, *8*, 1238.
[56] J. Huang, H. Sheng, R. D. Ross, J. Han, X. Wang, B. Song, S. Jin, *Nat. Commun.* **2021**, *12*, 3036.
[57] F. Lyu, Y. Bai, Q. Wang, L. Wang, X. Zhang, Y. Yin, *Dalton Trans.* **2017**, *46*, 10545.
[58] J. Chivot, L. Mendoza, C. Mansour, T. Pauporté, M. Cassir, *Corros. Sci.* **2008**, *50*, 62.
[59] X. Deng, K. Chen, H. Tüysüz, *Chem. Mater.* **2017**, *29*, 40.
[60] S. Gates-Rector, T. Blanton, *Powder Diffr.* **2019**, *34*, 352.